CHALMERS

Chalmers Publication Library

Effective dynamic properties of 3D composite materials containing rigid penny-shaped inclusions

(article starts on next page)

Effective dynamic properties of 3-D composite materials containing rigid penny-shaped inclusions

V.V. Mykhas'kiv [a]*, O.M. Khay [a], Ch. Zhang [b] and A. Boström [c]

[a] *Pidstryhach Institute for Applied Problems of Mechanics and Mathematics NASU, 79060 L'viv, Ukraine;* [b] *Department of Civil Engineering, University of Siegen, 57076 Siegen, Germany;* [c] *Department of Applied Mechanics, Chalmers University of Technology, 41296 Göteborg, Sweden*

Propagation of time-harmonic plane elastic waves in infinite elastic composite materials consisting of linear elastic matrix and rigid penny-shaped inclusions is investigated in this paper. The inclusions are allowed to translate and rotate in the matrix. First, the three-dimensional (3-D) wave scattering problem by a single inclusion is reduced to a system of boundary integral equations for the stress jumps across the inclusion-surfaces. A boundary element method (BEM) is developed for solving the boundary integral equations numerically. Far-field scattering amplitudes and complex wave numbers are computed by using the stress jumps. Then the solution of the single scattering problem is applied to estimate the effective dynamic parameters of the composite materials containing randomly distributed inclusions of dilute concentration. Numerical results for the attenuation coefficient and the effective velocity of longitudinal and transverse waves in infinite elastic composites containing parallel and randomly oriented rigid penny-shaped inclusions of equal size and equal mass are presented and discussed. The effects of the wave frequency, the inclusion mass, the inclusion density and the inclusion orientation or the direction of the wave incidence on the attenuation coefficient and the effective wave velocities are analyzed. The results presented in this paper are compared with the available analytical results in the low-frequency range.

Keywords: Composite materials; Rigid penny-shaped inclusions; Time-harmonic wave propagation; Effective wave velocity; Attenuation coefficient; Boundary integral equation method.

1. Introduction

Wave attenuation and dispersion in non-homogeneous composite materials have important applications in the ultrasonic non-destructive testing of composite materials, seismic events like earthquake analysis in geophysics etc. The theoretically predicted correlations between the wave velocities/attenuation and the geometrical/physical characteristics of distributed inclusions or inhomogeneities can be used for the interpretation and exploration of measured data and recorded events. In general, this problem requires an inverse solution procedure, which demands, however, the solution of the corresponding direct problem on the effects of the microstructure of the composite materials on their global dynamic behavior. This paper is devoted only to the direct problem instead of the inverse problem to estimate the effective dynamic properties of the composite materials.

The macroscopic dynamic properties of particulate elastic composites can be described by effective dynamic parameters of the equivalent homogeneous effective medium via a suitable homogenization procedure. Generally speaking, the homogenization procedure to determine the effective dynamic properties of particulate elastic composites is much more complicated than its static counterpart because of the inclusion interactions and multiple wave scattering effects. For small inclusion concentration or dilute inclusion distribution, their mutual interactions and the

multiple wave scattering effects can be neglected approximately. In this case, the theory of Foldy [1], the quasi-crystalline approximation of Lax [2] and their generalizations to the elastic wave propagation (e.g., Conoir and Norris [3], Gubernatis and Domany [4], Martin [5], Varadan et al. [6], Yang and Mal [7]) can be applied to determine the effective wave (phase) velocities and the attenuation coefficients in the composite materials with randomly distributed inclusions. In these models, wave scattering by a single inclusion has to be considered in the first step. Most previous publications on the subject have been focused on three-dimensional (3-D) elastic wave propagation analysis in composite materials consisting of an elastic matrix and spherical elastic inclusions (see Boström et al. [8], Kanaun and Levin [9], Kerr [10], Wei and Huang [11]). Aligned and randomly oriented ellipsoidal elastic inclusions have been considered by Berryman [12], Datta et al. [13], Kanaun and Levin [14], Ledbetter and Datta [15], Levin et al. [16], Sabina at al. [17] under the assumption that the wavelength is sufficiently long compared to the dimensions of the individual inclusions (quasi-static limit). As special cases, the results for a random distribution of cracks and penny-shaped inclusions can be derived from those for ellipsoidal inclusions. In the long wavelength approximation, analytical solutions for a single inclusion as a series of the wave number have been presented in these works. However, this approach is applicable only for low frequencies or small wave numbers. For moderate and high frequencies, numerical methods such as the finite element method or the boundary element method can be applied. By using the boundary integral equation method (BIEM) or the boundary element method (BEM) in conjunction with Foldy's theory the effective wave velocities and the wave attenuations in linear elastic materials with open and fluid-filled penny-shaped cracks as well as soft thin-walled circular inclusions have been calculated by Eriksson et al. [18], Zhang and Gross [19]. Both aligned and randomly oriented defect configurations have been studied, where a macroscopic anisotropy for aligned cracks and non-spherical inclusions appears. Previous results have shown that distributed crack-like defects may cause a decrease in the phase velocity and an increase in the wave attenuation. The efficiency and the applicability ranges of 2D homogenization analysis of elastic wave propagation through a random array of scatters of different shapes and dilute concentrations based on the BEM and Foldy-type dispersion relations were demonstrated also by many authors, for instance, by Maurel et al. [20], Sato and Shindo [21], Tourin et al. [22]. However, to the author's knowledge, the overall average dynamic response of 3D composite material containing randomly distributed and movable penny-shaped inclusions with a much larger rigidity than that of the matrix material has not been investigated for moderate and high frequencies.

In the present paper the effective medium concept is extended to the time-harmonic plane elastic wave propagation in an infinite linear elastic matrix with completely bonded rigid penny-shaped inclusions. Each inclusion is regarded as a rigid body and is allowed to translate and rotate in the matrix. The location of the micro-inclusions is assumed to be random, while their orientation is either aligned or completely random. To simplify the analysis, the radius and the mass of the distributed micro-inclusions are taken to be equal. Both time-harmonic plane longitudinal and transverse waves are considered in the analysis. The solution procedure consists of three steps. In the first step, the wave scattering problem is formulated as a system of boundary integral equations (BIEs) for the stress jumps across the inclusion surfaces. A boundary element method (BEM) is developed to solve the BIEs numerically, where the kinetics of the inclusion and the "square-root" singularity of the stress jumps at the inclusion edge are taken into account properly. The far-field scattering amplitudes of elastic waves induced by a single inclusion are calculated from the numerically computed stress jumps. In contrast to the work by Khay [23], where only the plane longitudinal wave was considered as the incident wave, here the general case of incident longitudinal and transverse waves is investigated and a regularization procedure for solving the BIEs is developed. It should be mentioned that the couples and the stress intensity factors for a single inclusion can be also computed on the base of BIEs solutions as presented by Dhaliwal et al [24], Kit et al. [25]. In the second step, the simple Foldy-type approximation [4] is utilized to calculate the complex effective wave numbers for a

dilute concentration of inclusions, where their interactions and multiple wave scattering can be neglected. Finally, the effective wave velocity and the attenuation coefficient are obtained by taking the real and the imaginary parts of the effective wave numbers. To investigate the influence of the wave frequency, the inclusion mass, the inclusion density, the inclusion orientation or the direction of the wave incidence on the effective dynamic parameters, several numerical examples for longitudinal and transverse elastic waves in infinite elastic composite materials with both parallel and randomly oriented inclusions are presented and discussed.

2. Scattering by a single inclusion: BIEs and BEM

We consider an elastic solid consisting of an infinite, homogeneous, isotropic and linearly elastic matrix specified by the mass density ρ, the shear modulus G and Poisson's ratio ν, and a rigid penny-shaped inclusion with the mass M, which occupies the domain S as shown in Fig. 1. The center of the Cartesian coordinate system $Ox_1x_2x_3$ coincides with the mass center of the inclusion and the values $x_3 = \pm 0$ correspond to the opposite interfaces between the matrix and the inclusion, where a welded contact is assumed. The stress-strain state in the solid is induced by a time-harmonic plane longitudinal L-wave or transverse T-wave with the frequency ω, the constant amplitude U_0, the phase velocities c_L and c_T, and the wave numbers $\chi_L = \omega/c_L$ and $\chi_T = \omega/c_T$, respectively. The displacement vector $\mathbf{u}^{in}(u_1^{in}, u_2^{in}, u_3^{in})$ of the incident wave is given by

$$\mathbf{u}^{in}(\mathbf{x}) = \mathbf{U}\exp\left[i\chi(\mathbf{n}\cdot\mathbf{x})\right]. \tag{1}$$

Here and hereafter the common factor $\exp(-i\omega t)$ is omitted, χ is the wave number of the incident wave, $\mathbf{n} = (\sin\theta_0, 0, \cos\theta_0)$ is the direction of propagation of the incident wave, θ_0 is the angle characterizing the direction of the wave incidence, and $\mathbf{U}$ is the polarization vector with $\chi = \chi_L$ and $\mathbf{U} = U_0\cdot\mathbf{n}$ for the L-wave and $\chi = \chi_T$, $\mathbf{U} = U_0\cdot\mathbf{e}$ and $\mathbf{n}\cdot\mathbf{e} = 0$ for the T-wave.

By using the superposition principle, the total displacement field $\mathbf{u}^{tot}$ in the solid can be written in the form

$$\mathbf{u}^{tot}(\mathbf{x}) = \mathbf{u}^{in}(\mathbf{x}) + \mathbf{u}(\mathbf{x}), \tag{2}$$

where $\mathbf{u}(u_1, u_2, u_3)$ is the unknown displacement vector of the scattered wave, which satisfies the equations of motion and the radiation conditions at infinity (see Achenbach [26]).

The inclusion is regarded as a rigid unit and its motion is described by the translation $\mathbf{u}^0(u_1^0, u_2^0, u_3^0)$ and the rotation with respect to the coordinate axes with the angles Ω_1, Ω_2 and Ω_3, respectively. Then the displacement components in the domain S can be represented by

$$u_j(\mathbf{x}) = -u_j^{in}(\mathbf{x}) + u_j^0 + (-1)^j\Omega_3 x_{3-j}, \qquad j = 1, 2,$$

$$u_3(\mathbf{x}) = -u_3^{in}(\mathbf{x}) + u_3^0 + \Omega_1 x_2 - \Omega_2 x_1, \qquad \mathbf{x}(x_1, x_2, \pm 0) \in S. \tag{3}$$

In order to obtain the integral representations for the displacement components we apply the Betty-Rayleigh reciprocity theorem in conjunction with the properties of the elastodynamic fundamental solutions. As a result, the displacement components of the scattered waves can be written in the form [25]:

$$u_j(\mathbf{x}) = \frac{1}{4\pi G}\iint_S \left\{\Delta\sigma_j(\xi)\frac{\exp(i\chi_T|\mathbf{x}-\xi|)}{|\mathbf{x}-\xi|} - \frac{1}{\chi_T^2}\frac{\partial}{\partial x_j}\left[\Delta\sigma_1(\xi)\frac{\partial}{\partial x_1} + \Delta\sigma_2(\xi)\frac{\partial}{\partial x_2} + \right.\right.$$

$$+\Delta\sigma_3\left(\boldsymbol{\xi}\right)\frac{\partial}{\partial x_3}\Bigg]\Bigg[\frac{\exp\left(i\chi_L\left|\mathbf{x}-\boldsymbol{\xi}\right|\right)}{\left|\mathbf{x}-\boldsymbol{\xi}\right|}-\frac{\exp\left(i\chi_T\left|\mathbf{x}-\boldsymbol{\xi}\right|\right)}{\left|\mathbf{x}-\boldsymbol{\xi}\right|}\Bigg]\Bigg\}dS_{\boldsymbol{\xi}}, \qquad j=1,2,3, \tag{4}$$

where use is made of the displacement continuity condition across the inclusion, $\left|\mathbf{x}-\boldsymbol{\xi}\right|$ is the distance between the field point $\mathbf{x}(x_1,x_2,x_3)$ and integration point $\boldsymbol{\xi}(\xi_1,\xi_2)$, and $\Delta\sigma_j$ ($j=1,2,3$) are the jumps of the interfacial stresses across the inclusion, which are defined by

$$\Delta\sigma_j(\mathbf{x})=\sigma_{j3}^-(\mathbf{x})-\sigma_{j3}^+(\mathbf{x}), \qquad j=1,2,3, \qquad \mathbf{x}\in S, \qquad \sigma_{j3}^{\pm}(\mathbf{x})=\lim_{x_3\to\pm0}\sigma_{j3}(\mathbf{x}). \tag{5}$$

Equation (5) together with the equation of motion of the inclusion as a rigid unit yields the following relations between the translations and the rotations of the inclusion and the stress jumps $\Delta\sigma_j$:

$$u_j^0=\frac{1}{\omega^2 M}\iint_S\Delta\sigma_j\left(\boldsymbol{\xi}\right)dS_{\boldsymbol{\xi}}, \qquad j=1,2,3,$$

$$\Omega_j=\frac{(-1)^{j+1}}{\omega^2 M\,i_j^2}\iint_S\xi_{3-j}\,\Delta\sigma_3\left(\boldsymbol{\xi}\right)dS_{\boldsymbol{\xi}}, \qquad j=1,2, \tag{6}$$

$$\Omega_3=\frac{1}{\omega^2 M\,i_3^2}\iint_S\left[\xi_1\,\Delta\sigma_2\left(\boldsymbol{\xi}\right)-\xi_2\,\Delta\sigma_1\left(\boldsymbol{\xi}\right)\right]dS_{\boldsymbol{\xi}},$$

where i_j is the radius of inertia of the inclusion with respect to the x_j-axis.

The displacement components in the matrix and the kinematical parameters of the inclusion are related to the stress jumps across the inclusion by the relations (4) and (6). Substitution of Eqs. (4) and (6) into Eq. (3) results in a system of three boundary integral equations (BIEs) for the stress jumps as

$$\iint_S\Delta\sigma_3\left(\boldsymbol{\xi}\right)R_3\left(\mathbf{x},\boldsymbol{\xi}\right)dS_{\boldsymbol{\xi}}=-4\pi G\chi_T^2\,u_3^{in}\left(\mathbf{x}\right), \qquad \mathbf{x}\in S,$$

$$\iint_S\left[\Delta\sigma_j\left(\boldsymbol{\xi}\right)R_j\left(\mathbf{x},\boldsymbol{\xi}\right)+\Delta\sigma_{3-j}\left(\boldsymbol{\xi}\right)R_{j(3-j)}\left(\mathbf{x},\boldsymbol{\xi}\right)\right]dS_{\boldsymbol{\xi}}=-4\pi G\chi_T^2\,u_j^{in}\left(\mathbf{x}\right), \quad j=1,2, \quad \mathbf{x}\in S. \tag{7}$$

In Eq. (7), the kernels R_j, R_{12} and R_{21} have the form

$$R_j\left(\mathbf{x},\boldsymbol{\xi}\right)=L_1\left(\left|\mathbf{x}-\boldsymbol{\xi}\right|\right)-\frac{\left(x_j-\xi_j\right)^2}{\left|\mathbf{x}-\boldsymbol{\xi}\right|^2}L_2\left(\left|\mathbf{x}-\boldsymbol{\xi}\right|\right)-\frac{4\pi\rho}{M}\left(1+\frac{\xi_{3-j}x_{3-j}}{i_3^2}\right), \qquad j=1,2,$$

$$R_3\left(\mathbf{x},\boldsymbol{\xi}\right)=L_1\left(\left|\mathbf{x}-\boldsymbol{\xi}\right|\right)-\frac{4\pi\rho}{M}\left(1+\frac{\xi_1 x_1}{i_2^2}+\frac{\xi_2 x_2}{i_1^2}\right),$$

$$R_{ij}\left(\mathbf{x},\boldsymbol{\xi}\right)=-\frac{\left(x_1-\xi_1\right)\left(x_2-\xi_2\right)}{\left|\mathbf{x}-\boldsymbol{\xi}\right|^2}L_2\left(\left|\mathbf{x}-\boldsymbol{\xi}\right|\right)+\frac{4\pi\rho}{M}\frac{\xi_i x_j}{i_3^2}, \quad i,j=1,2, \quad i\neq j, \tag{8}$$

$$L_i\left(r\right)=l_{i1}\left(r\right)\frac{\exp\left(i\chi_L r\right)}{r^3}-l_{i2}\left(r\right)\frac{\exp\left(i\chi_T r\right)}{r^3}, \quad i=1,2,$$

$$l_{11}\left(r\right)=1-i\chi_L r, \quad l_{12}\left(r\right)=1-i\chi_T r-\chi_T^2 r^2,$$

$$l_{21}\left(r\right)=3-3i\chi_L r-\chi_L^2 r^2, \quad l_{22}\left(r\right)=3-3i\chi_T r-\chi_T^2 r^2.$$

The boundary value problem governed by the BIEs (7) can be divided into an antisymmetric problem and a symmetric problem. The antisymmetric problem corresponding to the transverse motion of the inclusion is described by first equation of the BIEs (7) for the stress jump $\Delta\sigma_3$. After the solution of this equation the displacement u_3^0 and the rotations Ω_1 and Ω_2 can be obtained by using the relations (6). The symmetric problem corresponds to the motion of the inclusion in its own plane, which is governed by the last two equations of the BIEs (7) for the stress jumps $\Delta\sigma_1$ and $\Delta\sigma_2$. After these quantities have been computed by solving these equations, the kinematical parameters u_1^0, u_2^0 and Ω_3 can be obtained by using the relations (6).

The kernels of the BIEs (7) contain weakly singular integrals only. To isolate these singularities explicitly we rewrite the BIEs (7) as

$$A\iint_S \frac{\Delta\sigma_3(\xi)}{|\mathbf{x}-\xi|}dS_\xi + \iint_S \Delta\sigma_3(\xi)\left[\frac{1}{\chi_T^2}R_3(\mathbf{x},\xi) - \frac{A}{|\mathbf{x}-\xi|}\right]dS_\xi = -4\pi G u_3^{in}(\mathbf{x}), \quad \mathbf{x}\in S,$$

$$\iint_S \frac{\Delta\sigma_j(\xi)}{|\mathbf{x}-\xi|}\left[A - B\frac{\left(x_j-\xi_j\right)^2}{|\mathbf{x}-\xi|^2}\right]dS_\xi - B\iint_S \Delta\sigma_{3-j}(\xi)\frac{\left(x_1-\xi_1\right)\left(x_2-\xi_2\right)}{|\mathbf{x}-\xi|^3}dS_\xi +$$

$$+\iint_S \left\{\Delta\sigma_j(\xi)\left[\frac{1}{\chi_T^2}R_j(\mathbf{x},\xi) - \frac{A}{|\mathbf{x}-\xi|} + B\frac{\left(x_j-\xi_j\right)^2}{|\mathbf{x}-\xi|^3}\right] + \Delta\sigma_{3-j}(\xi)\left[\frac{1}{\chi_T^2}R_{j(3-j)}(\mathbf{x},\xi)+\right.\right. \tag{9}$$

$$\left.\left.+B\frac{\left(x_1-\xi_1\right)\left(x_2-\xi_2\right)}{|\mathbf{x}-\xi|^3}\right]\right\}dS_\xi = -4\pi G u_j^{in}(\mathbf{x}), \qquad j=1,2, \quad \mathbf{x}\in S,$$

where

$$A = \left(1+\gamma^2\right)/2, \quad B = \left(\gamma^2-1\right)/2, \quad \gamma^2 = (1-2\nu)/\left[2(1-\nu)\right].$$

In Eq. (9), the last integrals on the left-hand sides exist in the ordinary sense. This fact follows from an analysis of the integrand in the limit $\xi\to\mathbf{x}$. Therefore, in the numerical evaluation of these integrals it is sufficient to perform the integration over $S_\mathbf{x}^0$ by excluding a small region (the neighborhood of the $\mathbf{x}$-point) around $\mathbf{x}$ from S.

The singularities of the BIEs (9) are identical to those of the corresponding BIEs for the static inclusion problems, which have been investigated by Khaj [27] for the antisymmetric case and Rahman [28] for the symmetric case. The local behavior of the stress jumps at the front of the inclusion is also the same as in the static case. For a circular penny-shaped inclusion, the stress jumps have a "square-root" singularity, which can be expressed as

$$\Delta\sigma_j(\mathbf{x}) = \frac{\beta_j(\mathbf{x})}{\sqrt{a^2-x_1^2-x_2^2}}, \quad j=1,2,3, \quad \mathbf{x}\in S, \tag{10}$$

where $\beta_j(\mathbf{x})$ are unknown smooth functions, and a is the radius of the inclusion.

Substitution of Eq. (10) into Eq. (9) results in a system of BIEs for the functions $\beta_j(\mathbf{x})$. These BIEs have a weak singularity $1/|\mathbf{x}-\xi|$ at the source point $\xi=\mathbf{x}$ and a "square-root" singularity at the edge of the inclusion. To regularize the singular BIEs, the following integral relations for the elastostatic kernels are utilized:

$$\iint_S \frac{\beta(\xi)}{\sqrt{a^2-\xi_1^2-\xi_2^2}\cdot|\mathbf{x}-\xi|}dS_\xi = \pi^2\beta(\mathbf{x}) + \iint_{S_\mathbf{x}^0} \frac{\beta(\xi)-\beta(\mathbf{x})}{\sqrt{a^2-\xi_1^2-\xi_2^2}\cdot|\mathbf{x}-\xi|}dS_\xi,$$

$$\iint_S \frac{\beta(\xi)}{\sqrt{a^2 - \xi_1^2 - \xi_2^2}} \cdot \frac{(x_j - \xi_j)^2}{|\mathbf{x} - \xi|^3} dS_\xi = \frac{\pi^2}{2}\beta(\mathbf{x}) + \iint_{S_\mathbf{x}^0} \frac{[\beta(\xi) - \beta(\mathbf{x})]}{\sqrt{a^2 - \xi_1^2 - \xi_2^2}} \cdot \frac{(x_j - \xi_j)^2}{|\mathbf{x} - \xi|^3} dS_\xi, \tag{11}$$

$$\iint_S \frac{\beta(\xi)}{\sqrt{a^2 - \xi_1^2 - \xi_2^2}} \cdot \frac{(x_1 - \xi)(x_2 - \xi_2)}{|\mathbf{x} - \xi|^3} dS_\xi = \iint_{S_\mathbf{x}^0} \frac{[\beta(\xi) - \beta(\mathbf{x})]}{\sqrt{a^2 - \xi_1^2 - \xi_2^2}} \cdot \frac{(x_1 - \xi_1)(x_2 - \xi_2)}{|\mathbf{x} - \xi|^3} dS_\xi,$$

where use is made of the integral identities, taken from [28],

$$\iint_S \frac{dS_\xi}{\sqrt{a^2 - \xi_1^2 - \xi_2^2}\,|\mathbf{x} - \xi|} = \pi^2,$$

$$\iint_S \frac{(x_1 - \xi_1)^i (x_2 - \xi_2)^j}{\sqrt{a^2 - \xi_1^2 - \xi_2^2}\,|\mathbf{x} - \xi|^3} dS_\xi = \begin{cases} \pi^2/2, & \text{when } i = 2, \ j = 0 \ \text{ or } \ i = 0, \ j = 2, \\ 0 & \text{when } i = 1, \quad j = 1. \end{cases} \tag{12}$$

Next we perform the following transformation of the variables:

$$\begin{cases} x_1 = a \sin y_1 \cos y_2, \\ x_2 = a \sin y_1 \sin y_2, \end{cases} \qquad \begin{cases} \xi_1 = a \sin \eta_1 \cos \eta_2, \\ \xi_2 = a \sin \eta_1 \sin \eta_2, \end{cases} \tag{13}$$

where $\mathbf{y}(y_1, y_2)$ and $\eta(\eta_1, \eta_2)$ are new variables in the rectangular domain $\tilde{S}:\{0 \le y_1, \eta_1 \le \pi/2;\ 0 \le y_2, \eta_2 \le 2\pi\}$. Equation (13) transforms the circular integration domain to a rectangular integration domain and eliminates the "square-root" singularity at the front of the inclusion corresponding to $\eta_1 = \pi/2$.

By applying Eqs. (11)-(13) to the BIEs (9) we obtain their regularized version as

$$A\tilde{\beta}_3(\mathbf{y})\left[\pi^2 - \iint_{S_\mathbf{y}^0} \frac{\sin \eta_1}{R(\mathbf{y}, \eta)} dS_\eta\right] + \frac{1}{\vartheta^2} \iint_{S_\mathbf{y}^0} \tilde{\beta}_3(\eta) \tilde{R}_3(\mathbf{y}, \eta) \sin \eta_1 dS_\eta =$$

$$= -4\pi G \tilde{u}_3^{in}(\mathbf{y}), \qquad \mathbf{y}(y_1, y_2) \in S,$$

$$\tilde{\beta}_j(\mathbf{y})\left\{A\left[\pi^2 - \iint_{S_\mathbf{y}^0} \frac{\sin \eta_1}{R(\mathbf{y}, \eta)} dS_\eta\right] - B\left[\frac{\pi^2}{2} - \iint_{S_\mathbf{y}^0} \Phi_j(\mathbf{y}, \eta) \sin \eta_1 dS_\eta\right]\right\} + \tag{14}$$

$$+ B\tilde{\beta}_{3-j}(\mathbf{y})\iint_{S_\mathbf{y}^0} \Psi(\mathbf{y}, \eta) \sin \eta_1 dS_\eta + \frac{1}{\vartheta^2} \iint_{S_\mathbf{y}^0}\left[\tilde{\beta}_j(\eta) \tilde{R}_j(\mathbf{y}, \eta) +\right.$$

$$\left. + \tilde{\beta}_{3-j}(\eta) \tilde{R}_{j(3-j)}(\mathbf{y}, \eta)\right] \sin \eta_1 dS_\eta = -4\pi G \tilde{u}_j^{in}(\mathbf{y}), \quad j = 1, 2, \quad \mathbf{y}(y_1, y_2) \in S,$$

where

$$\tilde{\beta}_j(\mathbf{y}) = \beta_j(\mathbf{x}), \quad \tilde{u}_j^{in}(\mathbf{y}) = u_j^{in}(\mathbf{x}), \quad \tilde{R}_j(\mathbf{y}, \eta) = a^3 R_j(\mathbf{x}, \xi), \quad j = 1, 2, 3,$$

$$\tilde{R}_{ij}(\mathbf{y}, \eta) = a^3 R_{ij}(\mathbf{x}, \xi),, \quad i, j = 1, 2, \quad i \ne j. \tag{15}$$

In Eq. (15), $\mathbf{x}$ and ξ are defined by Eq. (13), $\vartheta = \chi_T a$ is the normalized wave number of the T-wave, $\tilde{S}_\mathbf{y}^0$ is the mapping of the domain $S_\mathbf{x}^0$ due to the transformation (13) (in the domain $\tilde{S}_\mathbf{y}^0$ the points $\mathbf{y}$ and η do not coincide), and

$$R(\mathbf{y}, \eta) = \left[\sin^2 y_1 + \sin^2 \eta_1 - 2\sin y_1 \sin \eta_1 \cos(y_2 - \eta_2)\right]^{1/2},$$

$$\Phi_1(\mathbf{y},\boldsymbol{\eta}) = \left(\sin y_1 \cos y_2 - \sin \eta_1 \cos \eta_2\right)^2 \left[R(\mathbf{y},\boldsymbol{\eta})\right]^{-3}, \tag{16}$$

$$\Phi_2(\mathbf{y},\boldsymbol{\eta}) = \left(\sin y_1 \sin y_2 - \sin \eta_1 \sin \eta_2\right)^2 \left[R(\mathbf{y},\boldsymbol{\eta})\right]^{-3},$$

$$\Psi(\mathbf{y},\boldsymbol{\eta}) = \left(\sin y_1 \cos y_2 - \sin \eta_1 \cos \eta_2\right)\left(\sin y_1 \sin y_2 - \sin \eta_1 \sin \eta_2\right)\left[R(\mathbf{y},\boldsymbol{\eta})\right]^{-3}, \quad j=1,2.$$

For the discretization of the domain $\tilde{S}$, a boundary element mesh with equal-sized rectangular elements is used. For simplicity, constant elements are adopted in this analysis. By collocating the BIEs (14) at discrete points coinciding with the centroids of each element, a system of linear algebraic equations for discrete values of $\tilde{\beta}_j$ is obtained. After solving the system of linear algebraic equations numerically, the stress jumps $\Delta\sigma_j$ across the inclusion can be obtained by the using the relations (10) and (15).

The far-field quantities of the scattered elastic waves can be computed from the stress jumps $\Delta\sigma_j$. For this purpose we use the asymptotic relations for an observation point far away from the inclusion, namely $|\mathbf{x}-\boldsymbol{\xi}| \approx |\mathbf{x}| - (\mathbf{x}\cdot\boldsymbol{\xi})/|\mathbf{x}|$ and $|\mathbf{x}-\boldsymbol{\xi}|^{-1} \approx |\mathbf{x}|^{-1}$, when $|\mathbf{x}|\to\infty$. By substituting of these relations into the integral representation formula (4) and introducing the spherical coordinate system with the origin at the center of the inclusion as

$$x_1 = R\sin\theta\cos\varphi, \qquad x_2 = R\sin\theta\sin\varphi, \qquad x_3 = R\cos\theta, \qquad 0\le\theta,\varphi\le 2\pi, \tag{17}$$

the asymptotic expressions for the scattered radial u_R and tangential u_θ, u_φ displacements in the far-field are obtained in the form

$$u_R(R,\theta,\varphi) = \frac{\exp(i\chi_L R)}{4\pi R} F_L(\theta,\varphi), \qquad R\to\infty,$$

$$u_\theta(R,\theta,\varphi) = \frac{\exp(i\chi_T R)}{4\pi R} F_{TV}(\theta,\varphi), \qquad R\to\infty, \tag{18}$$

$$u_\varphi(R,\theta,\varphi) = \frac{\exp(i\chi_T R)}{4\pi R} F_{TH}(\theta,\varphi), \qquad R\to\infty.$$

Here, F_L, F_{TV}, and F_{TH} are the scattering amplitudes of the scattered spherical longitudinal, vertically polarized transverse, and horizontally polarized transverse waves, respectively. They are given by

$$F_L(\theta,\varphi) = \frac{\gamma^2}{G}\sum_{j=1}^{3} p_j \iint_S \Delta\sigma_j(\boldsymbol{\xi})\exp\left[-i\chi_L(\mathbf{p}\cdot\boldsymbol{\xi})\right]dS_{\boldsymbol{\xi}},$$

$$F_{TV}(\theta,\varphi) = \frac{1}{G}\sum_{j=1}^{3} r_j \iint_S \Delta\sigma_j(\boldsymbol{\xi})\exp\left[-i\chi_T(\mathbf{p}\cdot\boldsymbol{\xi})\right]dS_{\boldsymbol{\xi}}, \tag{19}$$

$$F_{TH}(\theta,\varphi) = \frac{1}{G}\sum_{j=1}^{3} \tau_j \iint_S \Delta\sigma_j(\boldsymbol{\xi})\exp\left[-i\chi_T(\mathbf{p}\cdot\boldsymbol{\xi})\right]dS_{\boldsymbol{\xi}},$$

where p_j, r_j, τ_j $(j=1,2,3)$ are the coordinates of the spherical unit vectors $\mathbf{p} = (\sin\theta\cos\varphi,\ \sin\theta\sin\varphi,\ \cos\theta)$, $\mathbf{r} = (\cos\theta\cos\varphi,\ \cos\theta\sin\varphi,\ -\sin\theta)$ and $\boldsymbol{\tau} = (-\sin\varphi,\ \cos\varphi,\ 0)$.

The forward scattering amplitudes are defined as the values of $F_Z(\theta,\varphi)$ $(Z=L,TV,TH)$ in the direction of the wave incidence, i.e., $F_Z(\theta_0,0)$.

Thus, the scattering problem of time-harmonic elastic waves by a rigid penny-shaped inclusion in the far-field is reduced to the numerical solution of the BIEs (14) and the subsequent computation of the scattering amplitudes by using Eq. (19), where the transformation or mapping relations (13) have to be considered.

3. Scattering by distributed inclusions: determination of the effective dynamic parameters

We consider now a statistical distribution of rigid penny-shaped micro-inclusions in the matrix. The location of the micro-inclusions is assumed to be random, while their orientation is either completely random or aligned. In the case of aligned inclusions, it is assumed that the inclusions are parallel to the $x_1 - x_2$-plane. The radius a and the mass M of the inclusions are assumed to be equal. The average response of the composite materials to the wave propagation is characterized by the geometrical dispersion and attenuation of waves due to the wave scattering process. To describe these phenomena within the coherent wave field, the dynamic properties of the composite can be modeled by a complex and frequency-dependent wave number $K(\omega)$ as

$$K(\omega) = \frac{\omega}{c^*(\omega)} + i\alpha(\omega), \qquad (20)$$

where $c^*(\omega)$ is the effective phase velocity and $\alpha(\omega)$ is the attenuation coefficient for the wave of corresponding mode. With Eq. (20), the amplitude of a plane time-harmonic elastic wave propagating in the $\mathbf{n}$-direction can be expressed as

$$\mathbf{u}(\mathbf{x}, \omega) = \mathbf{U} \exp\left[iK(\mathbf{n} \cdot \mathbf{x})\right] = \mathbf{U} \exp\left[-\alpha(\omega)(\mathbf{n} \cdot \mathbf{x})\right] \exp\left[i\omega(\mathbf{n} \cdot \mathbf{x})/c^*(\omega)\right] \qquad (21)$$

For low concentration of inclusions or small number density, the interaction or multiple scattering effects among the inclusions can be neglected. Under these assumptions the complex effective wave numbers K_Z $(Z = L, T)$ of plane L- and T-waves can be calculated by using the Foldy-type dispersion relation, which was extended to elastic waves in [4] and may be stated as

$$K_Z^2 = \chi_Z^2 + \varepsilon a^{-3} F_Z^*, \qquad Z = L, T. \qquad (22)$$

In Eq. (22), ε is the density parameter of the inclusions, εa^{-3} corresponds to the number density of inclusions of the same radius, i.e. the number of inclusions per unit volume, F_Z^* is the average forward scattering amplitude of the corresponding wave mode by a single inclusion. For randomly oriented inclusions of equal size and equal mass the average should be taken only over all possible inclusion orientations. It should be noted here that the average over all inclusion orientations is the same as the average over all directions of the wave incidence (to avoid the additional average over all wave polarizations for an incoming T-wave, we assume that the normal to the inclusions lie in the plane of incidence of the incoming TV- or TH-wave). Hence

$$F_Z^* = \frac{1}{2} \int_0^\pi F_Z(\theta_0, 0) \sin\theta_0 d\theta_0, \qquad Z = L, TV, TH, \qquad (23)$$

where θ_0 is the angle characterizing the direction of the wave incidence, and $F_Z(\theta_0, 0)$ are the forward scattering amplitudes given by Eq. (19). For computing effective wave numbers for parallel cracks by using Eq. (22), $F_L^*(\theta_0) = F_L(\theta_0, 0)$, $F_{TV}^*(\theta_0) = F_{TV}(\theta_0, 0)$ and $F_{TH}^*(\theta_0) = F_{TH}(\theta_0, 0)$ should be taken. It should be noted here that the approximation for the complex wave number (22) can be considered as a special case of the multiple wave scattering models of higher orders [3, 5-7], and it involves only the first order in the inclusion density and

is thus only valid for a dilute or small inclusion density. In the case of a large density or high concentration of inclusions, more sophisticated models such as the self-consistent approach or the multiple scattering models should be applied, to take the mutual dynamic interactions between individual inclusions into account.

Once the complex effective wave numbers K_Z have been determined via Eq. (22), the effective wave velocities c_Z^* and the attenuation coefficients α_Z of the plane L- and T-waves can be obtained by considering the definition (20). This results in

$$c_Z^*(\omega) = \frac{\omega}{\text{Re}\left[K_Z(\omega)\right]}, \quad \alpha_Z(\omega) = \text{Im}\left[K_Z(\omega)\right], \qquad Z = L, TV, TH. \tag{24}$$

It should be remarked here that Foldy's theory was derived for isotropic wave scattering, which is appropriate macroscopically for the configuration of randomly oriented inclusions. A composite solid with aligned (parallel) penny-shaped inclusions exhibits a macroscopic anisotropy, namely a transversal anisotropy. When an incident plane wave propagates in an arbitrary direction, this gives rise to a coupling between the L- and T-waves, and thus a change in the effective polarization vector. However, it is reasonable to apply Foldy's theory, when the wave propagation is along the principal axes because of the decoupling of the L- and T-waves. In this special case, wave propagation can be treated like in the isotropic case [15].

4. Numerical results

The method presented in the previous sections is used to calculate the effective dynamic parameters of a composite elastic solid with both parallel and randomly oriented rigid penny-shaped inclusions for the propagation of time-harmonic plane L- or TV-waves. For numerical discretization of the inclusion surface, the domain $\tilde{S}$ is divided into 264 rectangular elements of length $\Delta y_1 = \pi/22$ and $\Delta y_2 = \pi/12$ in the y_1- and y_2-directions, the domain $\tilde{S}_\mathbf{y}^0$ is chosen as $\tilde{S}_\mathbf{y}^0 = \tilde{S} \setminus \Delta\tilde{S}_\mathbf{y}$, where $\Delta\tilde{S}_\mathbf{y}$ is the boundary element with the point $\mathbf{y}$ in the center of the element. Poisson's ratio is selected as 0.3, the radii of inertia of the circular inclusion are defined as $i_1 = i_2 = a/2$, $i_3 = a/\sqrt{2}$.

For comparison purpose, normalized mass, normalized effective wave velocities and normalized attenuation coefficients are introduced as $\bar{M} = M/(\rho a^3)$, $\bar{c}_Z = c_Z^*/c_Z$, $\bar{\alpha}_Z = 2a \cdot \alpha_Z/(\pi\varepsilon)$, where the subscript $Z = L, TV$ stands for L- and TV-waves respectively.

4.1. Parallel inclusions

For parallel or aligned penny-shaped inclusions, the macroscopic dynamic behavior of the composite materials is transversely isotropic. Thus, the effective wave velocities and the attenuation coefficient are dependent on the direction of the wave incidence. In this analysis, only two wave incidence directions are considered, namely normal incidence ($\theta_0 = 0^\circ$) of L- and T-waves and grazing incidence ($\theta_0 = 90^\circ$) of L- wave. This choice provides the zero-rotations of inclusions.

For normal incidence of a plane L-wave, the normalized attenuation coefficient $\bar{\alpha}_L$ and the normalized effective wave velocity $\bar{c}_L$ versus the dimensionless wave number ϑ are presented in Figs. 2 and 3. To study the effects of the inclusion mass and the inclusion density, two separate parametrical studies are performed. In the first case, the inclusion density parameter is fixed as $\varepsilon = 0.01$ and the inclusion mass is varied as $\bar{M} = 5$, 10, 15 and 20. In the second case, the inclusion mass is fixed as $\bar{M} = 10$ while the inclusion density parameter is varied as $\varepsilon = 0.01$,

0.05, 0.1 and 0.15. To check the accuracy of the implemented BEM, the present numerical results are compared with the analytical low-frequency solutions of Kanaun and Levin [14] given in the Appendix. Here and hereafter a very good agreement between both results is observed in the frequency range $0 \le \vartheta \le 0.3$.

In the low frequency range, the normalized attenuation coefficient $\bar{\alpha}_L$ increases rapidly with increasing ϑ, after reaching a maximum it then decreases and approaches its high frequency limit. An exception is noted in the case $\bar{M} = 5$, i.e., the lightest inclusions, where $\bar{\alpha}_L$ increases monotonically with increasing ϑ and approaches its high-frequency limit. For a fixed inclusion density parameter $\varepsilon = 0.01$, the peak value of $\bar{\alpha}_L$ increases with increasing mass $\bar{M}$ of the inclusions and it is shifted to a smaller value of the dimensionless frequency as $\bar{M}$ becomes larger. For a fixed value of the inclusion mass $\bar{M} = 10$, the peak value of the normalized attenuation coefficient $\bar{\alpha}_L$ decreases with increasing inclusion density parameter ε. The normalized attenuation coefficient $\bar{\alpha}_L$ in the high-frequency or short-wave limit does not depend on the frequency, the inclusion mass and the inclusion density. In the high-frequency limit $\bar{\alpha}_L$ is constant but the attenuation coefficient α_L is proportional to the inclusion density parameter ε by the relation $\bar{\alpha}_L = 2a \cdot \alpha_L / (\pi \varepsilon)$. Also, the inclusions are unmovable in the high-frequency limit and the normalized attenuation coefficient $\bar{\alpha}_L$ can be obtained by using the Kirchhoff approximation for short waves (see Achenbach [26]).

Figure 3 shows the effects of the inclusion mass $\bar{M}$ and the inclusion density parameter ε on the normalized effective wave velocity $\bar{c}_L$. For a fixed inclusion density parameter $\varepsilon = 0.01$, the normalized effective wave velocity $\bar{c}_L$ in the composite with light inclusions is smaller than that in the homogeneous matrix material, while an opposite tendency is observed in the case of heavy inclusions, for instance for $\bar{M} = 20$ and $\vartheta > 1$. For a fixed inclusion mass $\bar{M} = 10$, the normalized effective wave velocity $\bar{c}_L$ is smaller than that in the matrix material and its minimum value decreases with increasing inclusion density parameter ε. The high-frequency limit $\bar{c}_L \to 1$ at $\vartheta \to \infty$ means that the velocity of the L-wave in the short-wave limit coincides with that in the matrix. The explanation of this high-frequency limit follows from the geometrical optical interpretation of the wave field. The wave field at high frequencies may be considered as a set of independent beams propagating through the medium. Because of the existing continuous matrix material, the effective wave velocity should coincide with the wave velocity in the matrix in the high-frequency limit. It should be mentioned also that the low-frequency approximations of the effective wave velocities are non-dispersive (see Appendix).

The corresponding numerical results for grazing incidence of a plane L-wave are presented in Figs. 4 and 5. The normalized attenuation coefficient $\bar{\alpha}_L$ shows a similar dependence on the dimensionless wave number ϑ, the inclusion mass $\bar{M}$ and the inclusion density parameter ε, except for the case $\varepsilon = 0.01$ and $\bar{M} = 5$. For the same ε- and $\bar{M}$-values, the peaks of $\bar{\alpha}_L$ are larger than that for normal incidence as shown in Fig. 2. The normalized effective wave velocity $\bar{c}_L$ for grazing incidence of a plane L-wave as shown in Fig. 5 is also very similar to Fig. 3. Compared to the normalized effective wave velocity $\bar{c}_L$ for a normal incidence of plane L-wave, the maximum effective wave velocity $\bar{c}_L$ is increased while its minimum value is decreased. Also in contrast to Fig. 3(b), the normalized effective wave velocity $\bar{c}_L$ is larger than that of the matrix material at high frequencies. In general, the quite tangled effects of the inclusions' stiffness and mass on the average phase velocity are observed at different frequencies. A similar complex behavior of the corresponding curves for the layered elastic structures was reported by Zakharenko [29].

For normal incidence of a plane T-wave (then TV- and TH-wave are the same), the numerical results for the normalized attenuation coefficient $\bar{\alpha}_T$ and the normalized effective wave velocity $\bar{c}_T$ are presented in Figs. 6 and 7 versus the dimensionless wave number ϑ. For fixed inclusion mass $\bar{M}$ and inclusion density parameter ε, the global behavior of the normalized attenuation coefficient $\bar{\alpha}_T$ and the normalized effective wave velocity $\bar{c}_T$ is very similar to that for grazing incidence (i.e. $\theta_0 = 90^\circ$) of plane L-wave as presented in Figs. 4 and 5. In comparison to the peak values of $\bar{\alpha}_L$ for normal and grazing incidence of a plane L-wave, the peak values of $\bar{\alpha}_T$ for an normal incidence of a plane T-wave are increased in the case of fixed $\bar{M}$ - and ε-parameters. The minimum values of the normalized effective wave velocity $\bar{c}_T$ are reduced compared to $\bar{c}_L$ for normal and grazing incidence of a plane L-wave and for the same $\bar{M}$ - and ε-parameters, while the maximum values of $\bar{c}_T$ lie between the $\bar{c}_L$-values for normal and grazing incidence of a plane L-wave.

4.2. Randomly oriented inclusions

In the case of randomly oriented micro-inclusions, the macroscopic dynamic behavior of the composite material is isotropic. Thus, the effective wave velocity and the attenuation coefficient do not depend on the direction of the wave incidence.

For an incident plane L-wave, the normalized attenuation coefficient $\bar{\alpha}_L$ and the normalized effective wave velocity $\bar{c}_L$ are presented in Figs. 8 and 9 versus the dimensionless wave number ϑ. A comparison of Figs. 8 and 9 with Figs. 2-5 for parallel inclusions shows a similar dependence of the $\bar{\alpha}_L$ and $\bar{c}_L$ on the dimensionless wave number ϑ, the inclusion mass $\bar{M}$ and the inclusion density parameter ε. As expected, the peak values of $\bar{\alpha}_L$ and $\bar{c}_L$ for randomly oriented penny-shaped inclusions are larger than that for parallel micro-inclusions with $\theta_0 = 0^\circ$ but smaller than that for parallel inclusions with $\theta_0 = 90^\circ$.

Finally, Figs. 10 and 11 show the corresponding results for the normalized attenuation coefficient $\bar{\alpha}_{TV}$ and the normalized effective wave velocity $\bar{c}_{TV}$ for an incident plane TV-wave. By comparing Figs. 10 and 11 with Figs. 6 and 7 for parallel inclusions it can be concluded that the effects of the dimensionless wave number ϑ, the inclusion mass $\bar{M}$ and the inclusion density parameter ε on the normalized attenuation coefficient $\bar{\alpha}_{TV}$ and the normalized effective wave velocity $\bar{c}_{TV}$ are very similar to that for parallel inclusions. In contrast to parallel inclusions, the variations of $\bar{\alpha}_{TV}$ and $\bar{c}_{TV}$ with the dimensionless wave number ϑ are rather complicated at low frequencies. For instance, the normalized attenuation coefficient $\bar{\alpha}_{TV}$ for $\varepsilon = 0.01$ and $\bar{M} = 20$ shows two distinct peaks, which are not observed in the case of parallel inclusions. The normalized attenuation coefficient $\bar{\alpha}_{TV}$ for randomly oriented inclusions is smaller than that for parallel inclusions with $\theta_0 = 0^\circ$, while the normalized effective wave velocity $\bar{c}_{TV}$ could be larger or smaller than that for parallel inclusions depending on the dimensionless wave number ϑ, the inclusion mass $\bar{M}$ and the inclusion density parameter ε.

5. Conclusions

Attenuation and dispersion of time-harmonic elastic waves in linear elastic composite materials consisting of a linear elastic matrix and rigid penny-shaped inclusions is analyzed in the present paper. Translations and rotations of the inclusions in the matrix are taken into account in the analysis. Wave scattering by a single penny-shaped inclusion is investigated by a boundary

element method (BEM) to obtain the stress jumps across the inclusion surfaces. Then, far-field scattering amplitudes of elastic waves are computed by using the stress jumps. To describe the average macroscopic dynamic properties of the composite materials with a random distribution of penny-shaped micro-inclusions, complex wave numbers are computed by the Foldy-type dispersion relations, from which the effective wave velocities and the wave attenuation can be obtained. The present analysis is appropriate for a dilute distribution of micro-inclusions, where the mutual inclusion interactions and the multiple scattering effects can be approximately neglected. Both longitudinal waves and transversal waves in an infinite elastic composite material with parallel and randomly oriented rigid penny-shaped inclusions of equal size and equal mass are considered in the analysis. To explore the effects of the wave frequency, the inclusion mass, the inclusion density and the inclusion orientation or the direction of the wave incidence on the attenuation coefficient and the effective wave velocities, several numerical examples are presented and discussed.

Appendix. Long wavelength approximation of effective dynamic characteristics.

For a dilute concentration of parallel rigid penny-shaped inclusions [14]:

$$c_L^* = c_L \left[1 + \frac{8}{3} \varepsilon \gamma^2 \left(\frac{2}{3+\gamma^2} + \frac{1}{1+\gamma^2} \right) \sin^4 \theta_0 - \frac{1}{4} \varepsilon \bar{M} \right],$$

$$c_{TV}^* = c_T \left[1 + \frac{2}{3} \varepsilon \left(\frac{2}{3+\gamma^2} + \frac{1}{1+\gamma^2} \right) \sin^2 2\theta_0 - \frac{1}{4} \varepsilon \bar{M} \right],$$

$$c_{TH}^* = c_T \left[1 + \frac{16}{3(3+\gamma^2)} \varepsilon \sin^2 \theta_0 - \frac{1}{4} \varepsilon \bar{M} \right],$$

$$\alpha_L = \frac{\gamma^4}{12\pi a} \varepsilon \vartheta^4 \left\{ \frac{256}{45\gamma} \left[\frac{4(3+2\gamma^5)}{(3+\gamma^2)^2} + \frac{1+4\gamma^5}{(1+\gamma^2)^2} \right] \sin^4 \theta_0 + \frac{1}{4} \left(\frac{1}{2} + \frac{1}{\gamma^3} \right) \bar{M}^2 \right\},$$

$$\alpha_{TV} = \frac{1}{12\pi a} \varepsilon \vartheta^4 \left\{ \frac{64}{45} \left[\frac{4(3+2\gamma^5)}{(3+\gamma^2)^2} + \frac{1+4\gamma^5}{(1+\gamma^2)^2} \right] \sin^2 2\theta_0 + \frac{1}{4} \left(1 + \frac{\gamma^3}{2} \right) \bar{M}^2 \right\},$$

$$\alpha_{TH} = \frac{1}{12\pi a} \varepsilon \vartheta^4 \left[\frac{1024(3+2\gamma^5)}{45(3+\gamma^2)^2} \sin^2 \theta_0 + \frac{1}{4} \left(1 + \frac{\gamma^3}{2} \right) \bar{M}^2 \right],$$

For a dilute concentration of randomly oriented rigid penny-shaped inclusions [14]:

$$c_L^* = c_L \left[1 + \frac{64}{45} \varepsilon \gamma^2 \left(\frac{2}{3+\gamma^2} + \frac{1}{1+\gamma^2} \right) - \frac{1}{4} \varepsilon \bar{M} \right],$$

$$c_T^* = c_T \left[1 + \frac{8}{45} \varepsilon \left(\frac{12}{3+\gamma^2} + \frac{1}{1+\gamma^2} \right) - \frac{1}{4} \varepsilon \bar{M} \right],$$

$$\alpha_L = \frac{\gamma^4}{2\pi a} \varepsilon \vartheta^4 \left\{ \frac{1024}{2025\gamma} \left[\frac{4(3+2\gamma^5)}{(3+\gamma^2)^2} + \frac{1+4\gamma^5}{(1+\gamma^2)^2} \right] + \frac{1}{24} \left(\frac{1}{2} + \frac{1}{\gamma^3} \right) \bar{M}^2 \right\},$$

$$\alpha_T = \frac{1}{2\pi a}\varepsilon\vartheta^4\left\{\frac{128}{2025}\left[\frac{24(3+2\gamma^5)}{(3+\gamma^2)^2}+\frac{1+4\gamma^5}{(1+\gamma^2)^2}\right]+\frac{1}{24}\left(1+\frac{\gamma^3}{2}\right)\bar{M}^2\right\},$$

References

[1] L.L. Foldy, *Multiple scattering theory of waves*, Phys. Rev. 67 (1945), pp. 107-119.

[2] M. Lax, *Multiple scattering of waves-II*, Phys. Rev. 85 (1952), pp. 621-629.

[3] J.M. Conoir and A.N. Norris, *Effective wavenumbers and reflection coefficients for an elastic medium containing random configurations of cylindrical scatterers*, Wave Motion 47 (2010), pp. 183-197.

[4] J.E. Gubernatis and E. Domany, *Effects of microstructure on the speed and attenuation of elastic waves in porous materials*, Wave Motion 6 (1984), pp. 579-589.

[5] P.A. Martin, *Multiple Scattering: Interaction of Time-harmonic Waves with N Obstacles*, Cambridge, New York, 2006.

[6] V.K. Varadan, Y. Ma and V.V. Varadan, *Multiple scattering of compressional and shear waves by fiber-reinforced composite materials*, J. Acoust. Soc. Am. 80 (1986), pp. 333-339.

[7] R. Yang and A.K. Mal, *Multiple scattering of elastic waves in a fiber-reinforced composite*, J. Mech. Phys. Solids 42(1994), pp. 1945-1968.

[8] A. Boström, P. Olsson and S.K. Datta, *Effective plane wave propagation through a medium with spheroidal inclusions surrounded by thin interfacial layers*, Mech. Mat. 14 (1992), pp. 59-66.

[9] S.K. Kanaun and V.M. Levin, *Propagation of longitudinal elastic waves in composites with a random set of spherical inclusions*, Arch. Appl. Mech. 77 (2007), pp. 627-651.

[10] F.H. Kerr, *The scattering of a plane elastic wave by spherical elastic inclusions*, Int. J. Eng. Sci. 30 (1992), pp. 169-186.

[11] P.J. Wei and Z.P. Huang, *Dynamic effective properties of the particle-reinforced composites with the viscoelastic interphase*, Int. J. Solid. Struct. 41 (2004), pp. 6993-7007.

[12] J.G. Berryman, *Long-wavelength propagation in composite elastic media II: Ellipsoidal inclusions*, J. Acoust. Soc. Am. 68 (1980), pp. 1820-1831.

[13] S.K. Datta, H.M. Ledbetter and Y. Shindo, *Phase velocity and attenuation of plane elastic waves in a particle-reinforced composite medium*, Wave Motion 10 (1988), pp. 171-182.

[14] S.K. Kanaun and V.M. Levin, *Effective Field Method in Mechanics of Composite Materials*, Petrozavodsk University Press, Petrozavodsk, 1993 (in Russian).

[15] H.M. Ledbetter and S.K. Datta, *Effective wave speeds in an SiC-particle-reinforced Al composite*, J. Acous. Soc. Am. 79 (1986), pp. 239-248.

[16] V. Levin, M. Markov and S. Kanaun, *Propagation of long elastic waves in porous rocks with crack-like inclusions*, Int. J. Eng. Sci. 46 (2008), pp. 620-638.

[17] F.J. Sabina, V.P. Smyshlaev and J.R. Willis, *Self consistent analysis of waves in a matrix-inclusion composite I. Randomly oriented spheroidal inclusions*, J. Mech. Phys. Solids 41 (1993), pp. 1573-1588.

[18] A.S. Eriksson, A. Boström and S.K. Datta, *Ultrasonic wave propagation through a cracked solid*, Wave Motion 22 (1995), pp. 297-310.

[19] Ch. Zhang and D. Gross, *On Wave Propagation in Elastic Solids with Cracks*, Computational Mechanics Publications, Southampton, 1998.

[20] A. Maurel, J.F. Mercier and F. Lund, *Elastic wave propagation through a random array of dislocations*, Phys. Rev. B 70 (2004), pp. 024303 (1-15).

[21] H. Sato and Y. Shindo, *Influence of microstructure on scattering of pl;ane elastic waves by a distribution of partially debonded elliptical inclusions*, Mech. Mat. 34 (2002), pp. 401-409.

[22] A. Tourin, M. Fink and A. Derode, *Multiple scattering of sound*, Wav. Rand. Media 10 (2000), pp. R31-R60.

[23] O.M. Khay, *Scattering of harmonic waves by disk-shaped rigid inclusion in a three-dimensional elastic matrix*, Mech. Solids 43 (2008), pp. 910-918.

[24] R.S. Dhaliwal, B.M. Singh, J. Vrbik and A.P.S. Selvadurai, *Diffraction of torsional wave or plane harmonic compressional wave by an annular rigid disc*, Soil Dyn. Earthq. Eng. 3 (1984), pp. 150-156.

[25] H.S. Kit, V.V. Mykhas'kiv and O.M. Khay, *Analysis of the steady oscillations of a plane absolutely rigid inclusion in a three-dimensional elastic body by the boundary element method*, J. Appl. Math. Mech. 66 (2002), pp. 817-824.

[26] J.D. Achenbach, *Wave Propagation in Elastic Solids*, North-Holland Publishing Company, Amsterdam-London, 1973.

[27] M.V. Khaj, *Two-Dimensional Integral Equations of Newton Potential Type and Their Applications*, Naukova Dumka, Kyiv, 1993 (in Russian).

[28] M. Rahman, *Some problems of a rigid elliptical disk-inclusion bonded inside a transversely isotropic space*, J. Appl. Mech., ASME 66 (1999), pp. 612-630.

[29] A.A. Zakharenko, *Analytical studying the group velocity of three-partial Love (type) waves in both isotropic and anisotropic media*, Non-Destruct. Test. Eval. 20 (2005), pp. 237 − 254.
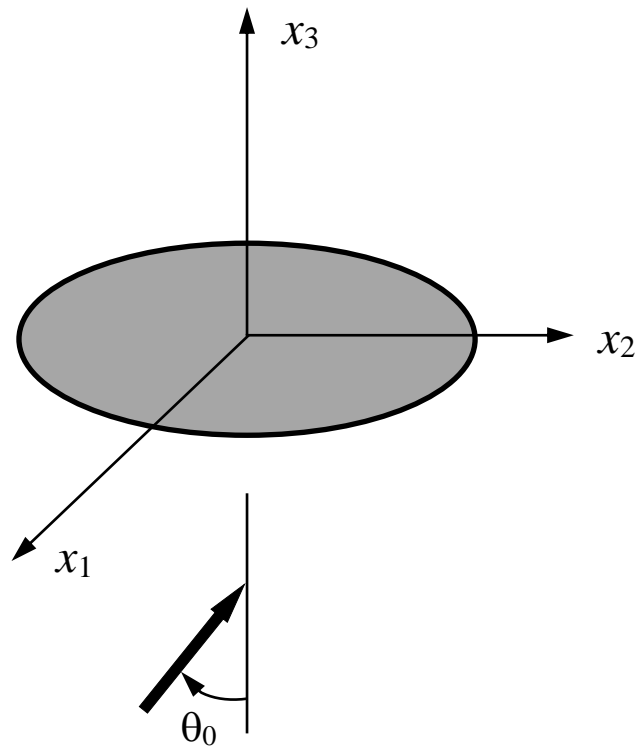
Fig. 1. A rigid penny-shaped inclusion in an elastic matrix.
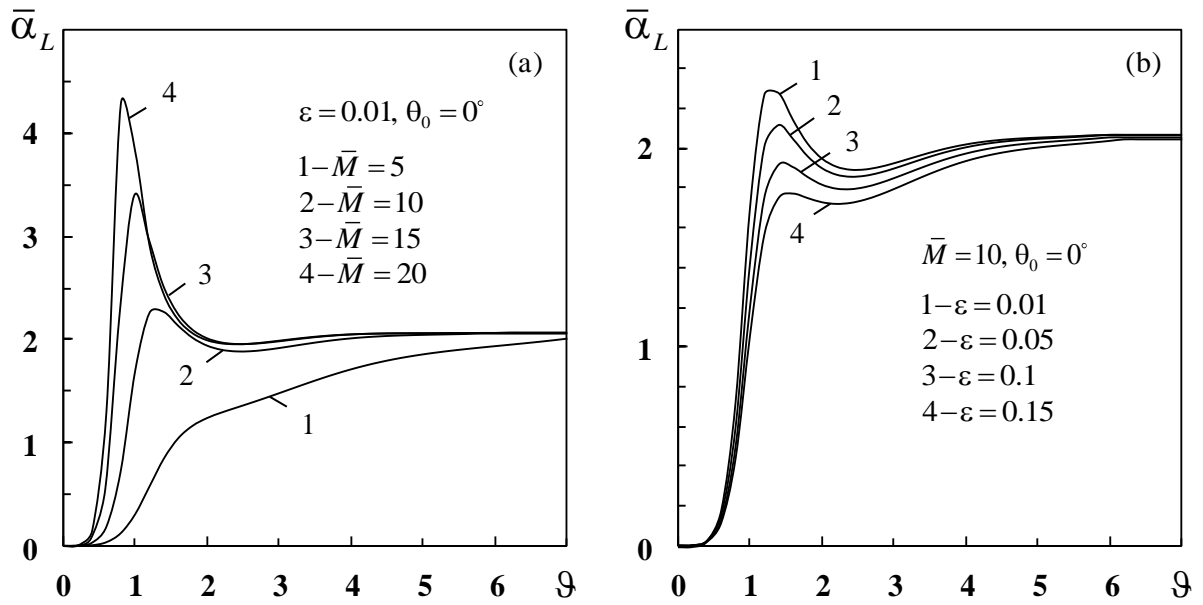
Fig. 2. Normalized attenuation coefficient versus the dimensionless wave number for parallel inclusions and normal *L*-wave incidence: (a) effects of the inclusion mass; (b) effects of the inclusion density.
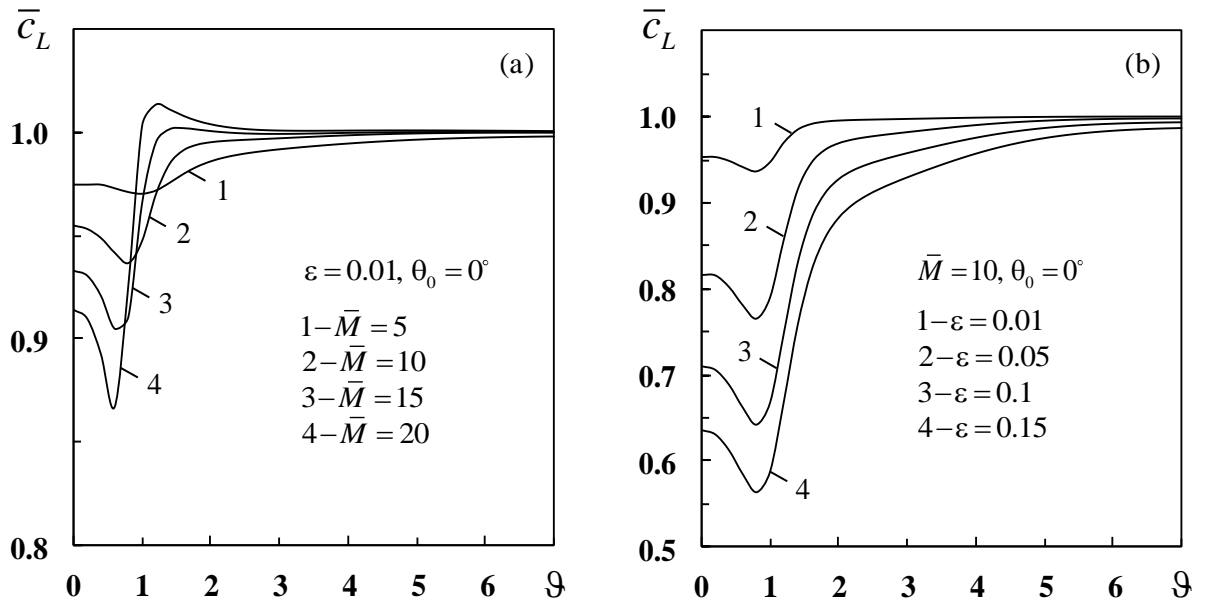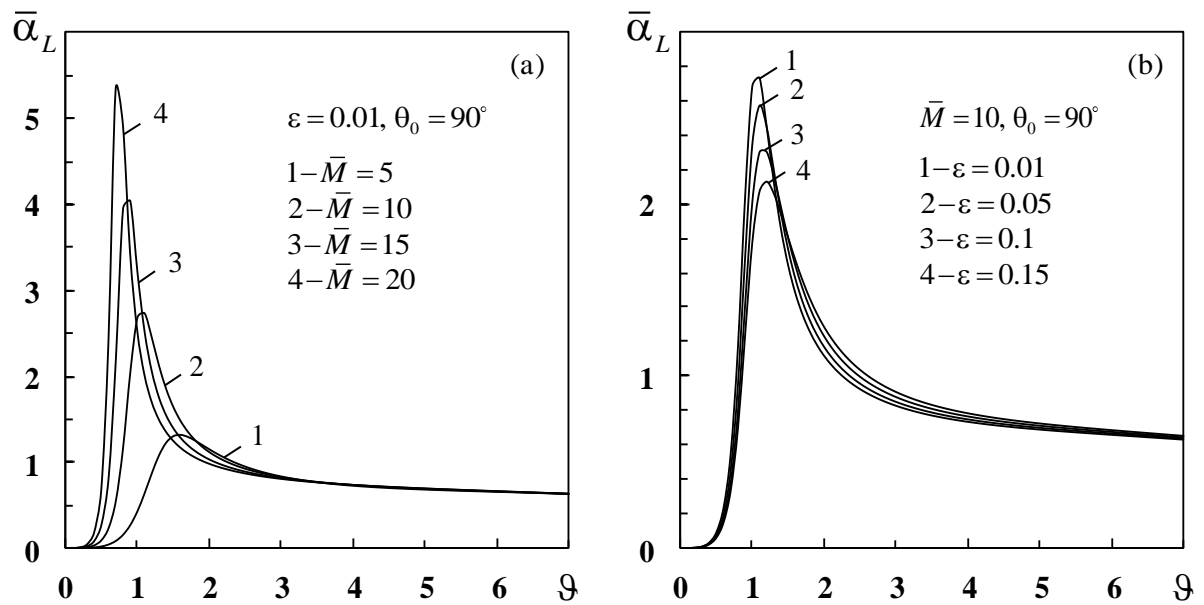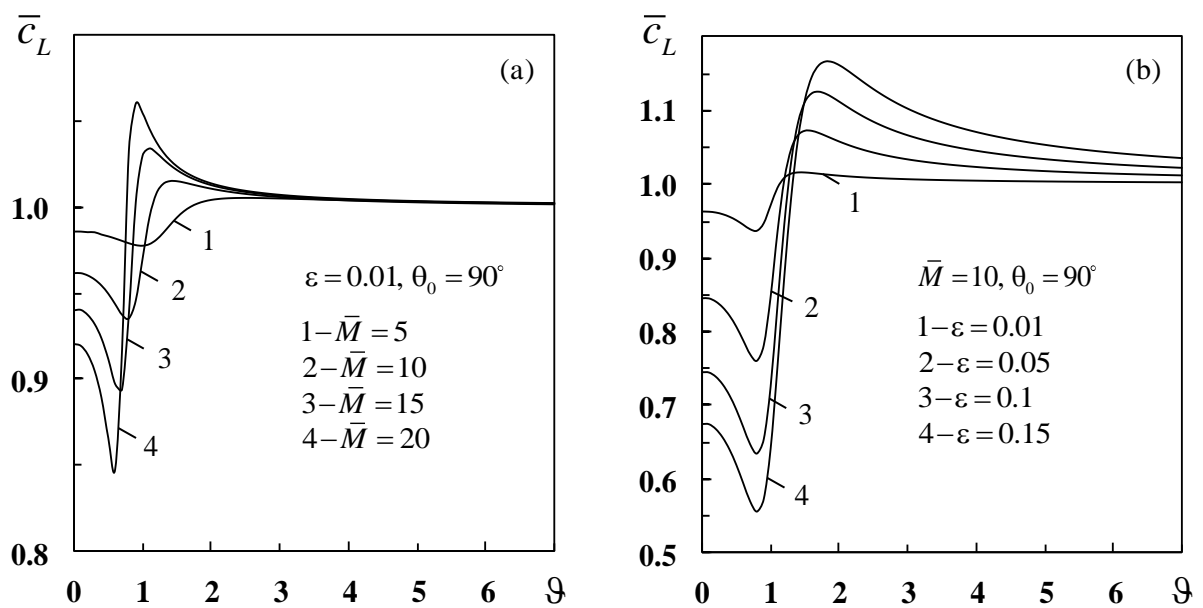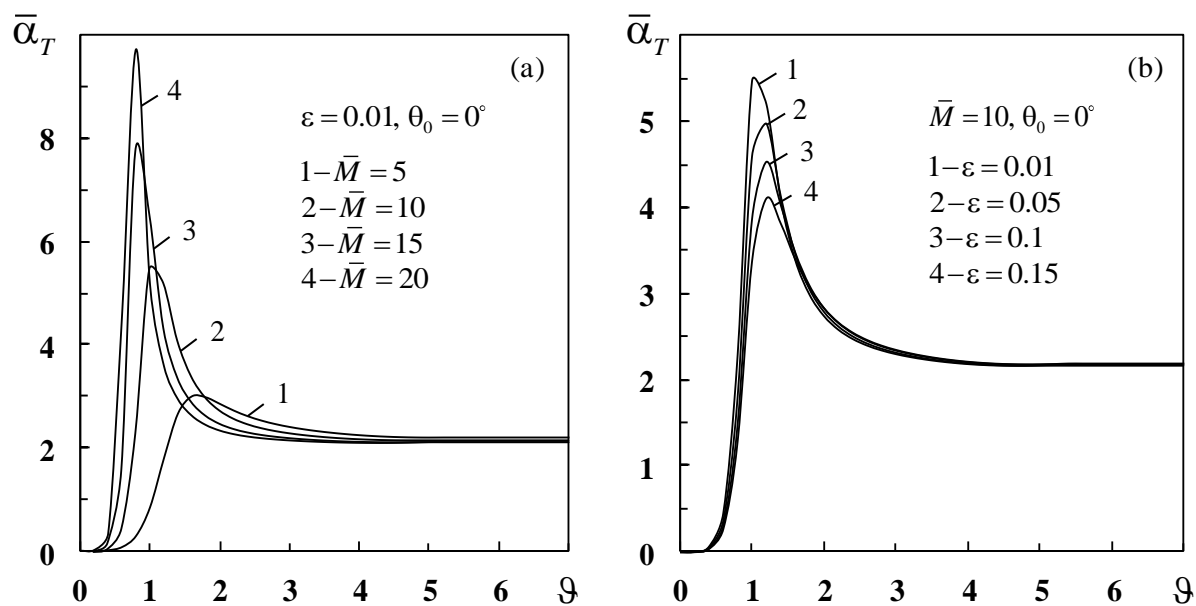

Fig. 3. Normalized effective wave velocity versus the dimensionless wave number for parallel inclusions and normal *L*-wave incidence: (a) effects of the inclusion mass; (b) effects of the inclusion density.
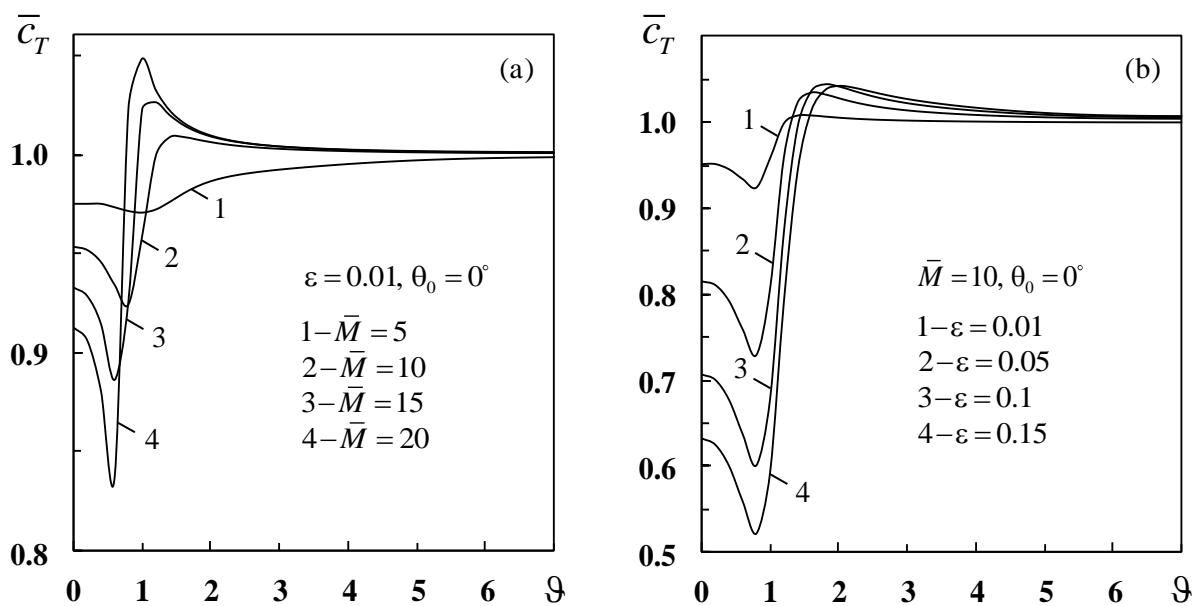
Fig. 4. Normalized attenuation coefficient versus the dimensionless wave number for parallel inclusions and grazing *L*-wave incidence: (a) effects of the inclusion mass; (b) effects of the inclusion density.

Fig. 5. Normalized effective wave velocity versus the dimensionless wave number for parallel inclusions and grazing *L*-wave incidence: (a) effects of the inclusion mass; (b) effects of the inclusion density.
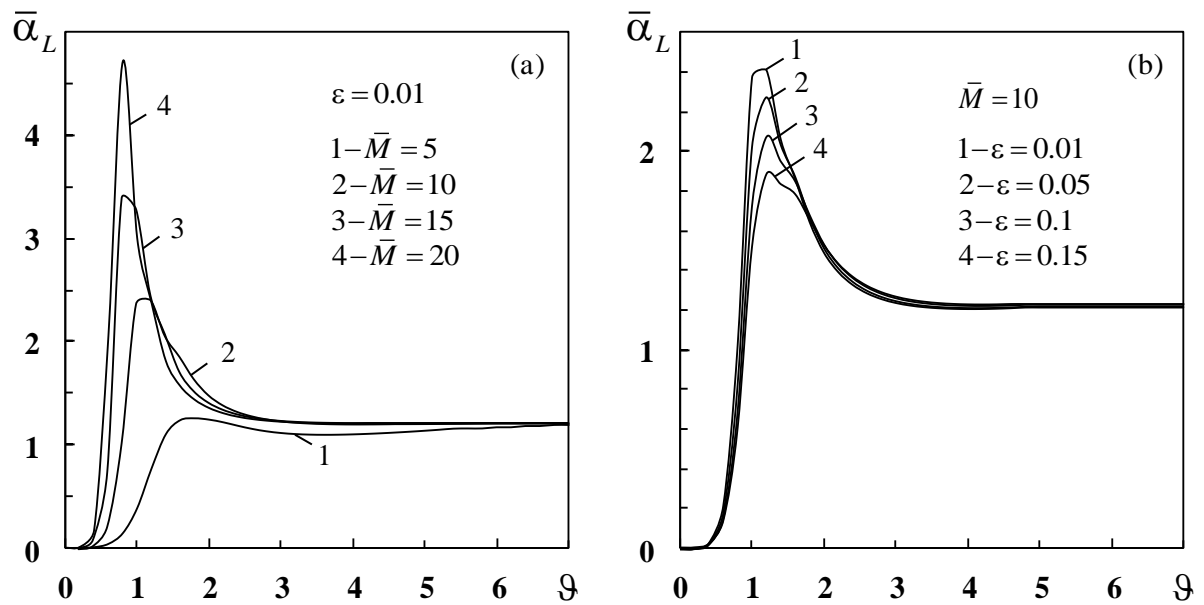
Fig. 6. Normalized attenuation coefficient versus the dimensionless wave number for parallel inclusions and normal *T*-wave incidence: (a) effects of the inclusion mass; (b) effects of the inclusion density.

Fig. 7. Normalized effective wave velocity versus the dimensionless wave number for parallel inclusions and normal *T*-wave incidence: (a) effects of the inclusion mass; (b) effects of the inclusion density.

Fig. 8. Normalized attenuation coefficient versus the dimensionless wave number for randomly oriented inclusions and *L*-wave incidence: (a) effects of the inclusion mass; (b) effects of the inclusion density.
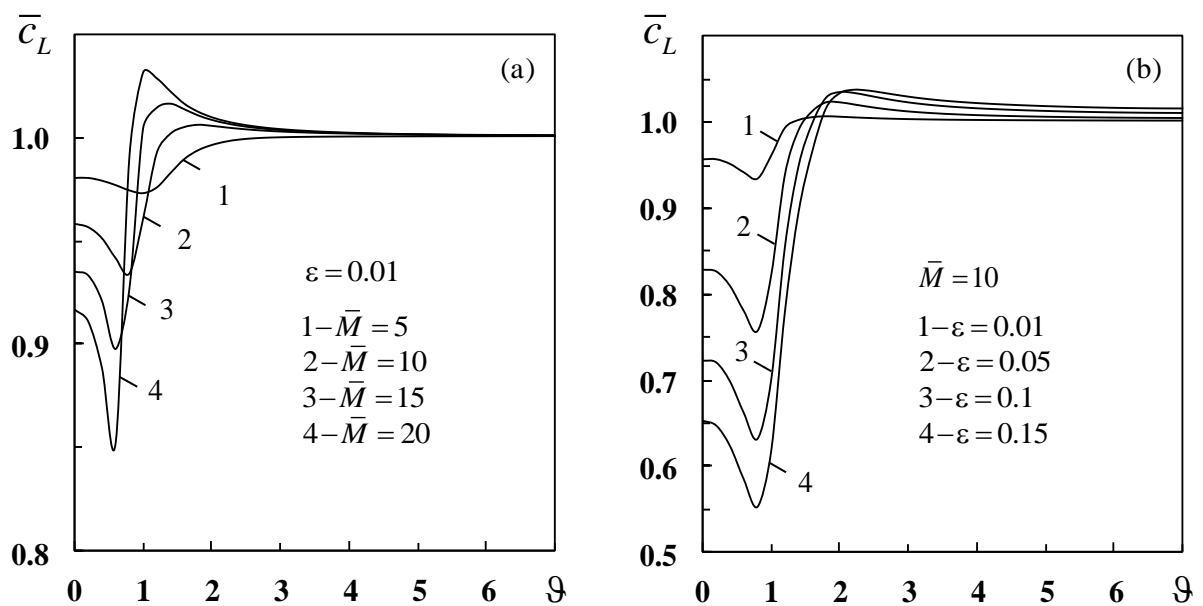

Fig. 9. Normalized effective wave velocity versus the dimensionless wave number for randomly oriented inclusions and *L*-wave incidence: (a) effects of the inclusion mass; (b) effects of the inclusion density.
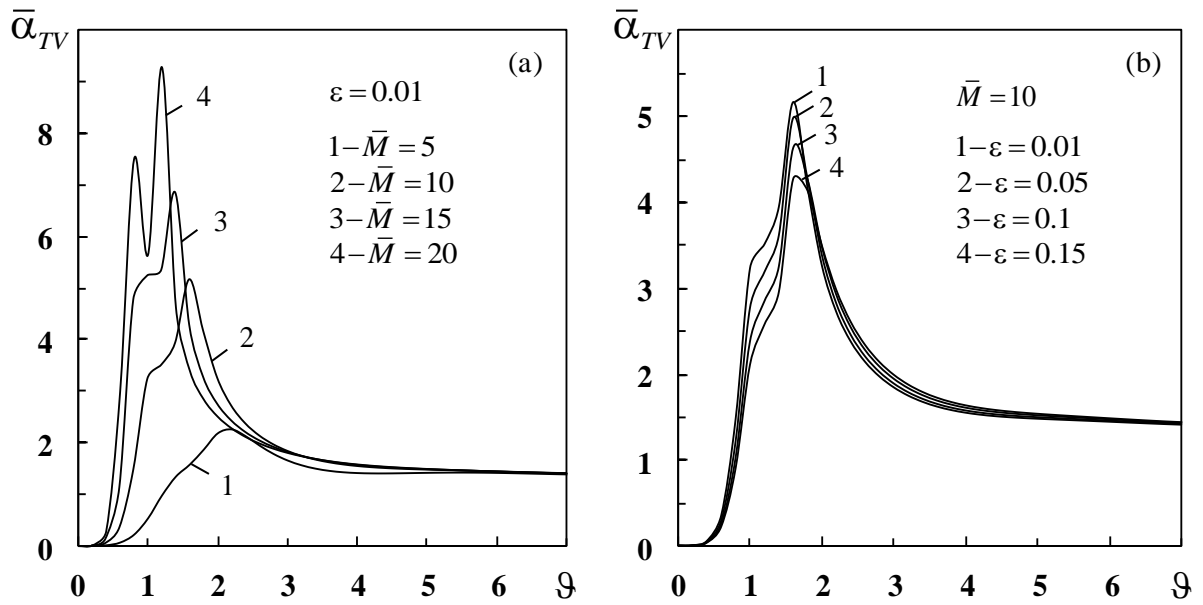
Fig. 10. Normalized attenuation coefficient versus the dimensionless wave number for randomly oriented inclusions and *TV*-wave incidence: (a) effects of the inclusion mass; (b) effects of the inclusion density.
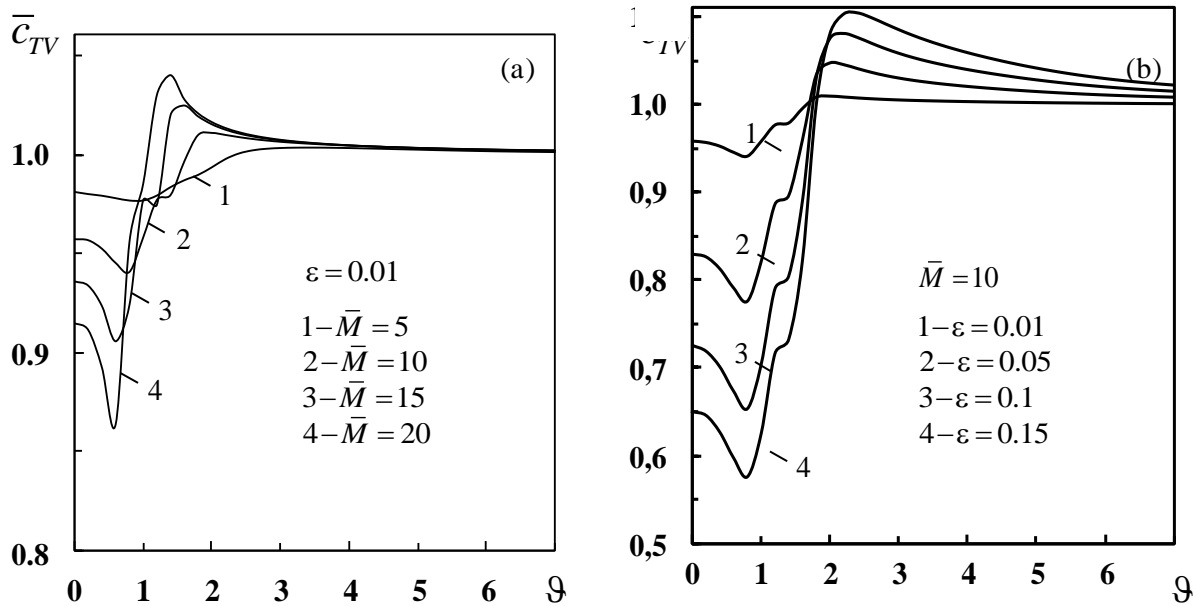

Fig. 11. Normalized effective wave velocity versus the dimensionless wave number for randomly oriented inclusions and *TV*-wave incidence: (a) effects of the inclusion mass; (b) effects of the inclusion density.